npj | 2D materials and applications

www.nature.com/npj2dmaterials

ARTICLE OPEN

Check for updates

Exciton spectroscopy and unidirectional transport in $MoSe_2$-WSe_2 lateral heterostructures encapsulated in hexagonal boron nitride

Dorian Beret[1,11], Ioannis Paradisanos[1,11], Hassan Lamsaadi[2,11], Ziyang Gan[3,11], Emad Najafidehaghani[3], Antony George[3,4], Tibor Lehnert[5,10], Johannes Biskupek[5], Ute Kaiser[5], Shivangi Shree[6], Ana Estrada-Real[1,7], Delphine Lagarde[1], Xavier Marie[1], Pierre Renucci[1], Kenji Watanabe[8], Takashi Taniguchi[9], Sébastien Weber[2], Vincent Paillard[2], Laurent Lombez[1]✉, Jean-Marie Poumirol[2]✉, Andrey Turchanin[3,4]✉ and Bernhard Urbaszek[1,7]✉

Chemical vapor deposition (CVD) allows lateral edge epitaxy of transition metal dichalcogenide heterostructures. Critical for carrier and exciton transport is the material quality and the nature of the lateral heterojunction. Important details of the optical properties were inaccessible in as-grown heterostructure samples due to large inhomogeneous broadening of the optical transitions. Here we perform optical spectroscopy of CVD grown $MoSe_2$-WSe_2 lateral heterostructures, encapsulated in hBN. Photoluminescence (PL), reflectance contrast and Raman spectroscopy reveal optical transition linewidths similar to high quality exfoliated monolayers, while PL imaging experiments uncover the effective excitonic diffusion length of both materials. The typical extent of the covalently bonded $MoSe_2$-WSe_2 heterojunctions is 3 nm measured by scanning transmission electron microscopy (STEM). Tip-enhanced, sub-wavelength optical spectroscopy mapping shows the high quality of the heterojunction which acts as an excitonic diode resulting in unidirectional exciton transfer from WSe_2 to $MoSe_2$.

npj 2D Materials and Applications (2022)6:84 ; https://doi.org/10.1038/s41699-022-00354-0

INTRODUCTION

Research on semiconducting transition metal dichalcogenide (TMDs) monolayers[1–3] and their heterostructures is motivated by collective effects of the electronic system[4–6] and the potential for emerging optoelectronic and quantum technology devices[7–17]. The optical and electronic properties of these materials can be tuned by combining different monolayers via van der Waals stacking to create vertical heterostructures[18–20]. But interestingly, tuning of optical properties of TMDs can also be achieved while staying in the ultimate monolayer limit. Recent progress is based on innovative growth techniques such as for Janus monolayers with different top and bottom chalcogen[21–24], as well as in lateral heterostructures (LHs)[25,26] within the monolayer plane with an atomically-sharp 1D interface which exhibits p-n junction characteristics[27,28]. Examples of potential applications for LHs are photodetectors[29], p-n junction diodes[25,30,31], photovoltaic[30], electroluminescent[30] and quantum devices[32].

LHs can be fabricated following one-step[25,26,28,31] or multiple-step[33,34] growth processes either by physical vapor deposition (PVD) or by chemical vapor deposition (CVD). Electron beam lithography has also been used for the fabrication of LHs[35]. One-step CVD approaches with suitable growth conditions are simpler and have the advantage to grow large area TMD LHs at lower temperatures[25]. Accessing the quality of the monolayer heterojunction is so far mainly based on electron microscopy techniques. A depletion width on the order of few nanometers is reported using scanning tunneling microscopy and spectroscopy techniques[36]. The electronic structures and band alignments of TMD LHs have been calculated using density functional theory[37] and the formation of interface excitons is predicted by tight-binding models, as well as effective mass models[38].

To further access carrier dynamics and excitonic properties at the interface optical spectroscopy is needed as a powerful and non-invasive tool. But in as-grown CVD samples details are masked due to the large inhomogeneous broadening reported for the optical transitions, mainly investigated at room temperature[26,28,30,31].

Here we perform optical spectroscopy and microscopy experiments in high quality CVD-grown $MoSe_2$-WSe_2 monolayer LHs[25]. We first lift the LHs from the growth substrate. This procedure shows that transfer of the LH to other substrates is possible for device processing. Second, we encapsulate the LHs in high quality exfoliated hBN flakes[39] (Fig. 1a). Encapsulation of the TMD monolayer in high quality hexagonal boron nitride (hBN)[39] is crucial to access the intrinsic optical properties of exfoliated and CVD grown flakes[40–48]. We report optical transition linewidth of the LH monolayer (≈5 meV at $T = 4$ K) comparable to high quality exfoliated layers. Our step-by-step scans across the heterojunctions in optical spectroscopy experiments show an abrupt change from WSe_2 to $MoSe_2$. In atomic-resolution transmission electron microscopy on our samples we find a transition with a nm-sharp

[1]Université de Toulouse, INSA-CNRS-UPS, LPCNO, 135 Avenue Rangueil, 31077 Toulouse, France. [2]CEMES-CNRS, Université de Toulouse, Toulouse, France. [3]Friedrich Schiller University Jena, Institute of Physical Chemistry, 07743 Jena, Germany. [4]Abbe Centre of Photonics, 07745 Jena, Germany. [5]Ulm University, Central Facility of Electron Microscopy, Group of Material Science Electron Microscopy, D-89081 Ulm, Germany. [6]Department of Physics, University of Washington, Seattle, WA, USA. [7]Institute of Condensed Matter Physics, Technische Universität Darmstadt, Darmstadt, Germany. [8]Research Center for Functional Materials, National Institute for Materials Science, 1-1 Namiki, Tsukuba 305-0044, Japan. [9]International Center for Materials Nanoarchitectonics, National Institute for Materials Science, 1-1 Namiki, Tsukuba 305-0044, Japan. [10]Present address: Karlsruhe Institute of Technology, Laboratory for Electron Microscopy, 76131 Karlsruhe, Germany. [11]These authors contributed equally: Dorian Beret, Ioannis Paradisanos, Hassan Lamsaadi, Ziyang Gan. ✉email: laurent.lombez@cnrs.fr; jean-marie.poumirol@cemes.fr; andrey.turchanin@uni-jena.de; bernhard.urbaszek@pkm.tu-darmstadt.de

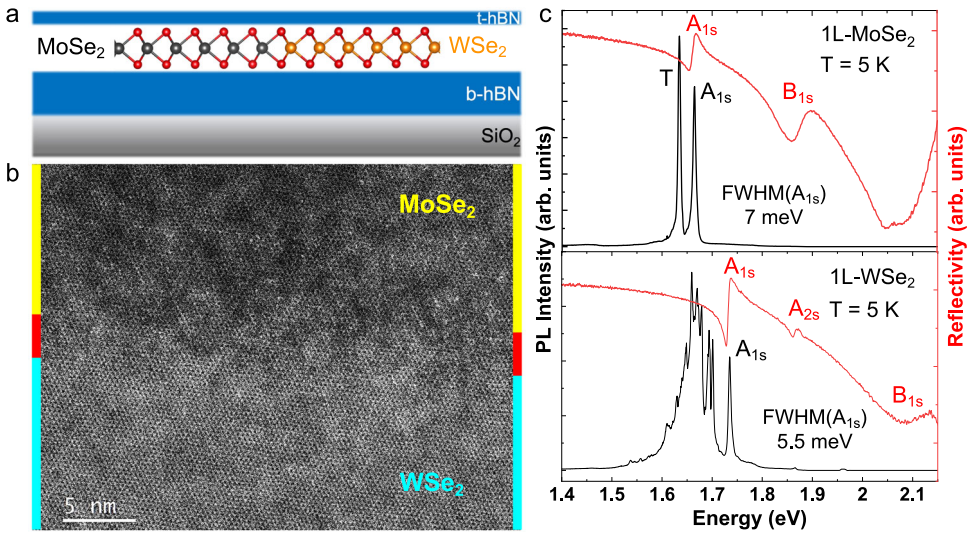

Fig. 1 Lateral heterostructure spectroscopy and microscopy. a Schematic representation of the $MoSe_2$-WSe_2 LH, encapsulated in hBN. Grey, orange and red spheres represent Mo, W and Se atoms, respectively. **b** HAADF-STEM image showing a $MoSe_2$-WSe_2 boundary (between the red lines). The $MoSe_2$ and WSe_2 areas are located between the yellow and the cyan lines, respectively. **c** Corresponding PL (black) and reflectance contrast (red) spectra of $MoSe_2$ (top) and WSe_2 (bottom). The PL linewidth of neutral excitons (A_{1s}) is 7 meV in $MoSe_2$ and 5.5 meV in WSe_2.

junction from $MoSe_2$ to WSe_2. The structural quality is also demonstrated in Raman spectroscopy. Photoluminescence (PL) imaging experiments allow us to investigate excitonic transport governed by the different effective lifetime of the exciton species for $MoSe_2$ and WSe_2 at $T = 4$ K and 300 K. We study exciton transport in sub-wavelength, tip-enhanced PL (TEPL) and Raman scattering (TERS) experiments at $T = 300$ K. Owing to our spatial resolution of 40 nm we uncover unidirectional exciton transport across the lateral heterojunction from WSe_2 to $MoSe_2$, that we model numerically.

RESULTS AND DISCUSSION

Sample preparation, electron microscopy and optical quality

Our $MoSe_2$-WSe_2 lateral monolayer heterojunction is grown by CVD synthesis that we reported recently[25]. A schematic representation of the encapsulated $MoSe_2$-WSe_2 structure is shown in Fig. 1a. Figure 1b shows high-angle annular dark field scanning transmission electron microscopy (HAADF-STEM) image recorded at the boundary region of the $MoSe_2$-WSe_2 structures. The image was recorded at an operating voltage of 200 kV, see supplement. The atomically resolved HAADF image allows the detection of the roughness of the interface at sub-nm resolution due to exploiting of the Z-contrast, where lighter Mo atoms show darker contrast than heavier W atoms[49]. Thus, $MoSe_2$ appears darker and WSe_2 appears brighter. From these measurements we estimate the transition width of the boundary region between $MoSe_2$ and WSe_2 to be as narrow as ≈3 nm. This sharp, high quality junction enables us to gain insights into exciton transport experiments across the heterojuntion with sub-wavelength resolution, see discussion below.

We use water-assisted deterministic transfer to pick up as-grown, CVD LHs using polydimethylsiloxane (PDMS) and deterministically transfer and encapsulate them in hBN[47,50]. We use these encapsulated samples for all optical spectroscopy measurements.

We first analyze the PL and differential white light reflectivity spectra of the individual monolayer areas (away from the heterojunction), collected at $T = 4$ K. Figure 1c shows superimposed PL (black) and reflectivity (red) spectra of $MoSe_2$ (top) and WSe_2 (bottom) monolayers after transfer and encapsulation in hBN. We measure in PL a neutral exciton (A_{1s}) linewidth of 7 meV in $MoSe_2$ and 5.5 meV in WSe_2 (Fig. 1c). These FWHM values are comparable to high-quality exfoliated $MoSe_2$ and WSe_2 monolayers[15,43–45]. $MoSe_2$ monolayers exhibit two pronounced PL emission peaks at 1.665 eV and 1.635 eV, assigned to neutral (A_{1s}) and charged (T) excitons, respectively[51]. In the case of WSe_2, the A_{1s} transition is located at 1.734 eV with the singlet trions (T) and dark excitons (X^D) lying 35 meV and 40 meV below A_{1s}, consistent with previous reports[52]. Additional peaks appear at lower energies, attributed to contributions from neutral, charged biexcitons and localized emission from defects[53,54]. At the heterojunction, additional low energy emission could be expected under certain conditions from the formation of interlayer excitons[38].

In Fig. 1c strong excitonic resonances appear in differential reflectivity for both materials with negligible Stokes shift in energy compared to the PL emission, which is a sign of negligible exciton localization effects for these spectra. Clear signatures of B_{1s} exciton states are also observed in both materials. For WSe_2 the appearance of the A_{2s} excited exciton state, which has a larger Bohr radius, shows the good quality of the CVD-grown monolayers of the LHs[55].

We collect the Raman, PL and reflectivity spectra within our detection spot while moving the sample over a ≈10 μm distance with a step size of ≈150 nm using attocube nanopositioners. Typical Raman PL and reflectivity scans across a heterojunction are shown in the contour plots of Fig. 2a–c. A black dashed line indicates the position of the heterojunction in each contour plot. As a common feature for all three contour plots, we observe abrupt changes in the optical spectra as we scan across the lateral heterojunction, as a result of distinctly different phonon energies and exciton transition energies in the two materials.

Now we discuss Raman spectroscopy results in Fig. 2a for monolayer $MoSe_2$ and WSe_2, collected at $T = 4$ K using an excitation laser wavelength of $\lambda = 633$ nm. The main Raman peaks of $MoSe_2$ and WSe_2 can be identified in the contour plot (detailed Raman spectra can be found in the Supplementary Material, section B). For monolayer $MoSe_2$ we observe the $A_1'(\Gamma)$ phonon at 241 cm^{-1} and the $E'(\Gamma)$ at 291 cm^{-1}[56], while a strong peak at 458 cm^{-1} has been associated to other peaks to form triplets[57].

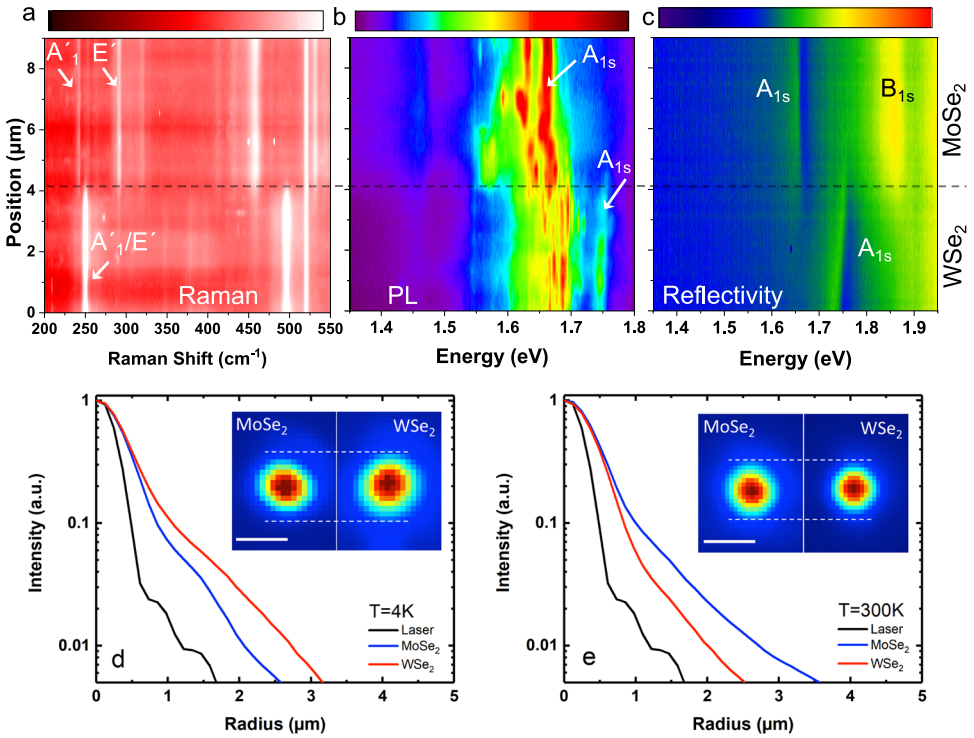

Fig. 2 Far field optical study. Contour plot of (**a**) Raman ($\lambda_L = 633$nm), (**b**) PL ($\lambda_L = 633$nm) and (**c**) white light reflectivity spectra scans across a WSe_2-$MoSe_2$ heterojunction at $T = 5$ K. The black horizontal dashed line indicates the position of the heterojunction. Color bars for panels (**a**), (**b**) and (**c**) are normalized from 0 to 1. **d** Exciton diffusion measurements at a temperature of $T = 4$ K for the $MoSe_2$ monolayer region (blue) and WSe_2(red). In the inset we show the $MoSe_2$ diffusion PL profile compared to the WSe_2 one. The laser intensity profile (black) is shown to indicate over which area excitons are initially generated, with small intensity oscillations due to Airy discs visible in logarithmic scale. **e** Same as **d** but at $T = 300$ K.

Interestingly, we also observe a strong peak at 531 cm^{-1}, recently assigned to multi-phonon processes associated with either both K and M point phonons or a combination of Γ point phonons[57]. The observation of this Raman peak is a signature of resonant excitation with an excited exciton state in $MoSe_2$. WSe_2 phonons are spectrally different compared to $MoSe_2$. The degenerate $A_1'(\Gamma)$/ $E'(\Gamma)$ phonons are located at 250 cm^{-1} and, similar to $MoSe_2$, a strong and recently discovered peak at 495 cm^{-1} is also observed here and attributed to multi-phonon processes at K and M points or combination of Γ point phonons[57].

The PL linescan in Fig. 2b shows emission from the main exciton transitions in WSe_2 and $MoSe_2$ (indicated by arrows) and a clear change in transition energy is discernible as we go across the lateral junction, with similar energies as for the individual spectra shown in Fig. 1c. Due to the extreme sensitivity of the PL emission energy spectrum on the defect concentration and dielectric environment[19], we see spectral shifts between spectra taken at different positions. This makes the PL contour plot appear less smooth than the Raman and reflectivity linescans.

The reflectivity linescan shown in Fig. 2c shows a clear change in the main exciton energies as we scan from one material to the other. The main neutral exciton A_{1s} feature in $MoSe_2$ in reflectivity is at an energy of 1.665 eV, whereas for WSe_2 this transition energy is clearly shifted to 1.734 eV. Reflectivity is less sensitive to the local defect and dielectric environment and therefore the measured transition energies remain comparatively constant from one spectrum to the other[19].

A PL imaging experiment is used to probe the effective diffusion length in the two TMD materials that are connected at the junction. First, we concentrate on results away from the lateral junction i.e. neither the excitation nor the PL emission profile have any spatial overlap with the lateral junction. The experiment consists in a local photogeneration of excitons with a He:Ne laser focused on a spot size of about 0.7 μm (see black curve in Fig. 2) and an excitation power of 5 μW. The generated spatial gradient of the exciton concentration (i.e. chemical potential gradient) induces lateral diffusion of excitons which is probed by recording the spatial PL profile with a CMOS camera, see supplement, where we integrate over the full spectral range of the monolayer emission. Figure 2d shows the PL profiles obtained at $T = 4$ K on WSe_2 (red line) and $MoSe_2$ (blue line). We clearly observe that PL emission occurs over a larger spot diameter than the laser excitation[58–60]. At this temperature WSe_2 shows a longer effective diffusion length than $MoSe_2$. This difference is also visible in the inset by directly comparing the images of the PL profile from the two materials.

Interestingly, this behavior is reversed at $T = 300$ K where $MoSe_2$ shows a longer effective diffusion length than WSe_2 (Fig. 3b). This is possibly linked to dark excitonic states which have longer lifetimes (PL emission times)[61,62]. Indeed, the lowest energy state of the conduction band is a dark state in WSe_2 while it is a bright state in $MoSe_2$. The PL intensity evolution with the temperature shows opposite trends: WSe_2 is darker at low temperature and brighter at room temperature as compared to $MoSe_2$[63]. The contribution of dark exciton states with longer lifetime would increase the effective diffusion length as compared to $MoSe_2$, as dark exciton emission is negligible for $MoSe_2$[64,65]. Therefore, when we compare the two materials WSe_2 has a longer diffusion length at 4 K and a shorter one at $T = 300$ K.

Near-field studies of the lateral heterojunction

Due to the extremely sharp nature of the junction (2–3 nm, see Fig. 1b) between the two materials, tip-enhanced Raman and PL spectroscopy are necessary to characterize the junction with sub-wavelength resolution. TEPL and TERS were carried out at room

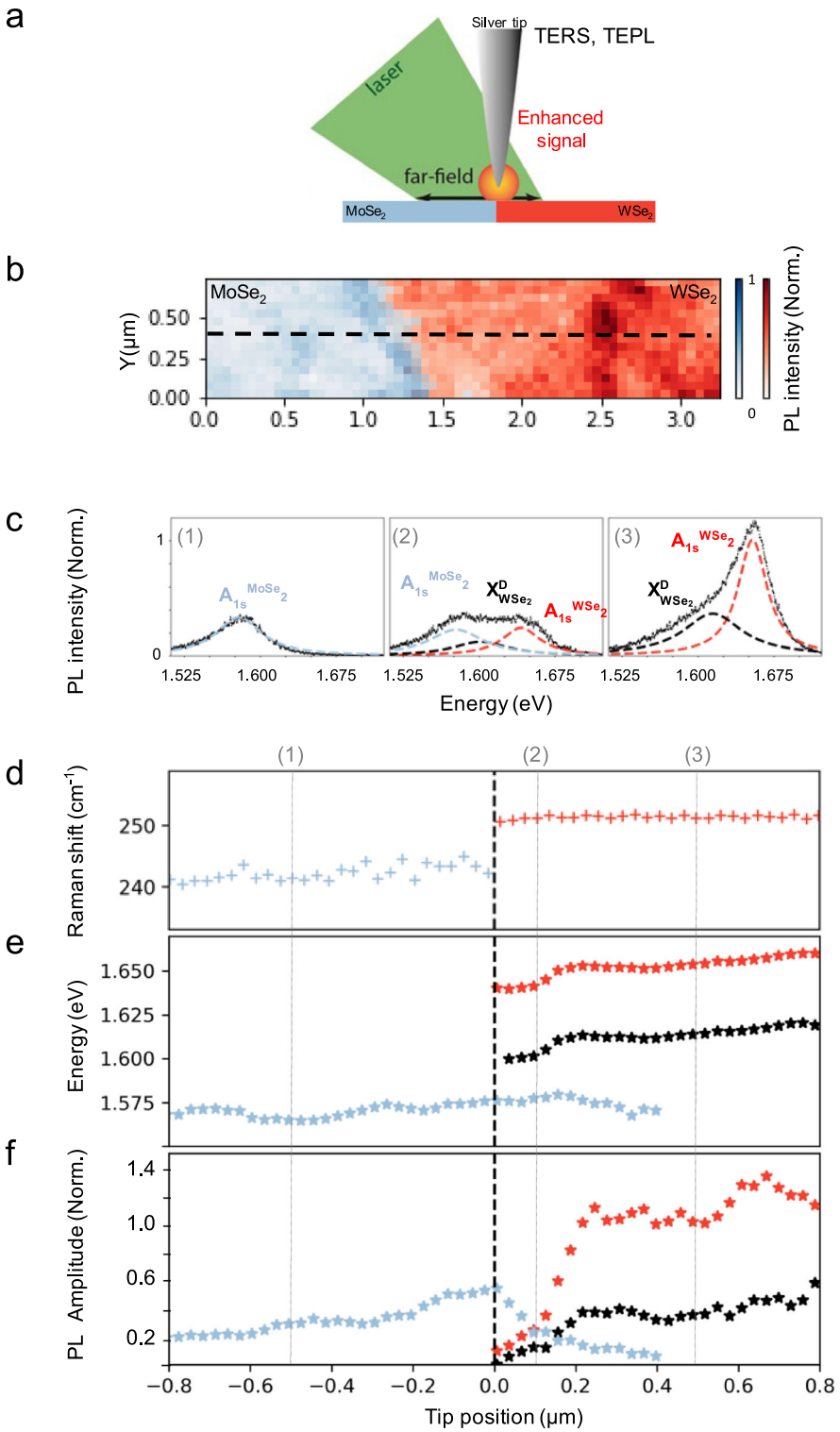

Fig. 3 Tip-enhanced spectroscopy of the $MoSe_2$-WSe_2 interface. a Schematic of the TEPL, TERS experimental set-up. **b** Spectrally integrated TEPL intensity colormap of the interface area. The red (respectively blue) color intensity is the value of integrated PL from 1.620 eV to 1.650 eV (respectively from 1.550 eV to 1.580 eV). **c** Typical TEPL spectra taken along the dashed line in **b**. Zone (1) on the left: 500 nm from the interface inside the $MoSe_2$ area ($x = -0.5$ μm). Zone (2) at the center: 100 nm from the interface inside the WSe_2 area ($x = 0.1$ μm). Zone (3) on the right: 500 nm from the interface inside the WSe_2 area ($x = 0.5$ μm). Three different excitonic components are observed in these curves: the WSe_2 neutral exciton($A_{1s}^{WSe_2}$), the dark (out-of-plane) exciton ($X_{WSe_2}^{D}$), and the $MoSe_2$ neutral exciton ($A_{1s}^{MoSe_2}$) and their respective contributions are used to fit the experimental data using individual Lorentzian function: red, black and light blue dashed lines respectively. **d** A′1(Γ) phonon wavenumber measured by TERS along the dashed line in **b** as a function of the tip position. **e** Energy of the individual Lorentzian peaks obtained from the fitting procedure displayed in **c**. **f** Amplitude of the individual Lorentzian peaks obtained from the fitting procedure displayed in **c**. In figure **d**, **e**, **f** the position of the interface appears as a vertical black dashed line. The positions where the PL spectra of **c** were taken appear as light vertical grey dashed lines.

temperature and the spatial resolution, determined by the tip diameter, is estimated to be ≈ 40 nm, far below the measured excitonic diffusion lengths we observed in the individual materials[66–68]. For TEPL (TERS) a 633 nm (532 nm) linearly polarized laser was focused onto the silver tip apex using a long working distance x100 objective (0.7 NA). The collection aperture is kept open to ensure that photons emitted a few micrometers away from the tip can be collected. The sample is scanned while recording PL spectra both with the tip in contact mode and 30 nm away from the surface. The near field contribution is then obtained by taking the difference between both recorded signals. Figure 3 shows a color map of the near field PL integrated intensity, excitation power was fixed to 0.4 mW and the sample scanning step size to 60 nm. The transition between WSe_2 and $MoSe_2$ can be clearly identified, and those images were used to select an interface region which gives uniform PL.

We then record PL spectra every 30 nm following the dashed line on the color map. Figure 3c displays three typical spectra measured at (1) 500 nm from the interface inside the $MoSe_2$ area, (2) at 100 nm from the interface inside the WSe_2 area and (3) at 500 nm from the interface inside the WSe_2 area. All measured PL spectra are fitted using a combination of the different excitonic contributions from $MoSe_2$ and WSe_2: the WSe_2 neutral exciton ($A_{1s}^{WSe_2}$) at about 1.66 eV (see dashed red line), the dark (out-of-plane) exciton ($X_{WSe_2}^{D}$) near 1.61 eV (see dashed black line), and the $MoSe_2$ neutral exciton ($A_{1s}^{MoSe_2}$) at about 1.57 eV (see dashed blue line), in agreement with the different transitions identified in the literature at room temperature[69]. Figure 3d–f show the results of the global fitting procedure of the PL spectra as a function of tip position. The position of the interface (see vertical dashed line) can be identified precisely thanks to the TERS spectra that show a sharp variation of the $A_1'(\Gamma)$ phonon energy at the interface. Figure 3e, f display the energy and amplitude of each component of the PL spectra as a function of the tip position. We find the same phonon wavenumbers and exciton transition energies in our near-field and far-field measurements.

We note that the energy of both bright and dark WSe_2 exciton are constant away from the interface but show a slight decrease when approaching the interface (≈200 nm), this could be an indication that tensile strain is present in the WSe_2 layer to account for the lattice mismatch at the junction with $MoSe_2$[70,71]. Scanning across the junction, the amplitude of both WSe_2 bright and dark exciton emission increases, going from zero at the interface to a plateau hundreds of nm away from the interface (see red and black stars in Fig. 3f). Importantly a clear contribution of the $MoSe_2$ bright exciton can be seen when tip-enhanced excitation happens deep inside the WSe_2 area (see light blue stars). The amplitude of this $A_{1s}^{MoSe_2}$ contribution is decreasing as the excitation (tip) moves away from the interface, reaching zero at 400 nm away from the interface in WSe_2.

This behavior indicates that excitons excited under the tip inside the WSe_2 area are diffusing through the interface and recombine inside the $MoSe_2$ area. Excitons are by consequence able to travel through 400 nm (roughly ten times our spatial resolution) of WSe_2 before reaching the interface. Interestingly this is not a symmetric phenomenon: we do not detect any WSe_2 related PL emission when the tip (and hence the optical excitation) is positioned inside the $MoSe_2$ area. This behavior shows that the junction acts as an exciton diode, allowing excitons to cross from WSe_2 to $MoSe_2$ but not the other way around. This non reciprocal behavior is in agreement with the excitonic energy landscape at the interface and previously observed behavior in far field measurement[72]. Indeed as illustrated in Fig. 4 a $A_{1s}^{WSe_2}$ is ≈90 meV above $A_{1s}^{MoSe_2}$ presenting a potential barrier that exciton cannot cross even at room temperature.

To get more quantitative understanding of measured exciton transport we perform numerical modeling of the experiment by solving a one-dimensional steady-state diffusion equation in the two materials and through the interface:

$$G(x) + D\frac{d^2n(x)}{dx^2} - \frac{n(x)}{\tau(x)} - \mu F(x)\frac{dn(x)}{dx} = 0 \quad (1)$$

Where $n(x)$ is the local excitons density, D the diffusion coefficient set to 1 cm^2/s and τ is the exciton lifetimes that we set to 200 ps and 150 ps for $MoSe_2$ and WSe_2 respectively. We consider a Gaussian generation profile under the tip given by $G(x) = G_0 \exp(-\frac{x^2}{w^2})$, where G_0 is the amplitude and w is the width of the Gaussian distribution (set to 40 nm, our effective tip diameter in the experiment).

A change in the exciton energy (i.e. chemical potential variation of the exciton) can act as an effective drift contribution that we simply model by adding an effective field μF in the equation (see Fig. 4a). The mobility is set to $\mu = 500\ cm^2/V/s$[58] and the F is set to 1 mV/nm. The latter value is taken sufficiently high to let the current flow only in one direction. Also the effective field is applied to a small region of 20 nm at the interface. Figure 4b displays the experimental spatially integrated PL value as a function the tip position. To ease the numerical modeling, the contributions of the bright and dark excitons in WSe_2 have been added and the PL intensity of each material has been normalized away from the junction. Figure 4c displays the results of the modeling when we spatially integrate the PL profiles. The inset shows the same modeling without considering the effective field $F = 0$ where a more symmetrical behavior is seen at the interface. The model reproduces the main experimental result: PL signal from $MoSe_2$ is seen when exciting WSe_2 up to 400 nm from the junction, whereas exciton transport in the other direction is not possible. This underlines that the junction acts as an excitonic diode (i.e. an excitonic current can only flow from WSe_2 to $MoSe_2$). Figure 4d presents the calculated PL intensity taken at the maximum of the PL profile. The main tendency is conserved but we see an increase of the PL intensity of $MoSe_2$ at the interface, indicating an accumulation of excitons as they cannot cross the junction. This PL intensity increase is also seen experimentally. The light density of states linked to the plasmonic resonance at the silver tip can possibly modify the exciton emission rate locally[73].

In conclusion, we have performed detailed spectroscopic studies on CVD grown lateral $MoSe_2$-WSe_2 heterostructures. As an important step towards device processing and for accessing the intrinsic optical quality of the junction, we have first transferred the sample from its original growth substrate and then encapsulated the lateral heterostructures in top and bottom flakes of high quality hBN. Our experiments give access to the excitonic structures at cryogenic temperatures, with neutral exciton transition linewidth of the order of 5 meV. In exciton diffusion experiments we show that the $MoSe_2$ and $WeSe_2$ exciton transport show opposite trends in temperature dependent experiments, as dark excitons contribute to the PL signal in WSe_2 and not in $MoSe_2$. Our near field optical study using tip-enhanced experiments shows the important role of the hetero-junction, as we measure that an excitonic current can only flow from WSe_2 to $MoSe_2$ and not the other way. This behavior is reproduced by a simple diffusion model where the exciton energy difference between the two materials acts as a barrier over a distance of a few nm. Our findings highlight the high structural quality of the heterojunction at the interface that can be regarded as an efficient excitonic diode, in the context of the broader research field of excitonic devices[11,74–76].

METHODS

We use water-assisted deterministic transfer to pick up as-grown, chemical vapor deposition (CVD) LHs using polydimethylsiloxane (PDMS) and deterministically transfer and encapsulate them in hBN[47,50]. Raman, PL and differential white light reflectivity spectra are collected at $T = 5$ K in a closed-loop liquid helium (LHe) system. For

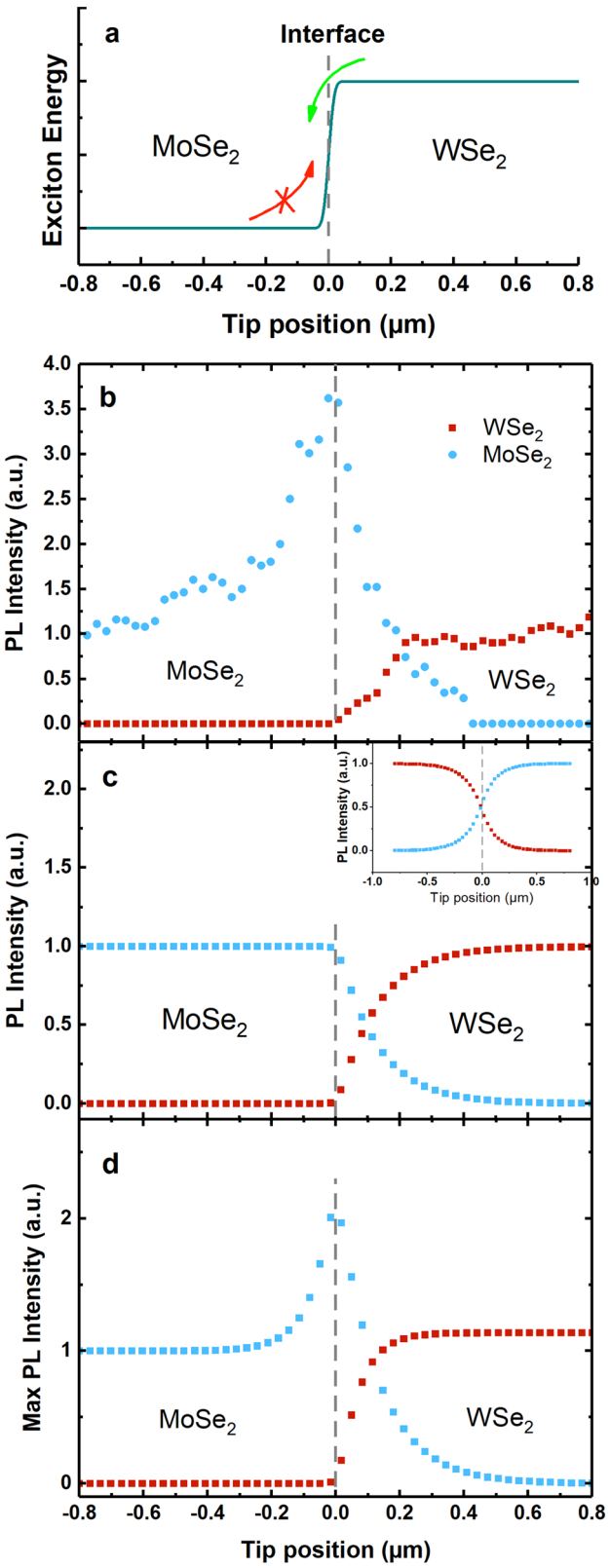

Fig. 4 Modeling near field optical spectrocopy of the junction. **a** Scheme of the exciton energy between the two materials. **b** Experimental values of the PL integrated intensity as a function of the tip position for the two materials. The bright and dark contributions in WSe_2 have been added and PL integrated intensities have been normalized away from the junction. **c** Modeling results of the spatially integrated PL intensity assuming a perfect collection of all photons. Inset: results without considering an energy difference at the junction. **d** Modeling results of the PL intensity at the maximum of the PL profile.

the Raman and PL experiments we use a 633 nm HeNe laser as an excitation source with a spot size diameter of ≈1μm and 6 μW power. In reflectivity we use a tungsten-halogen white light source with a power of a few nW to collect the intensity reflection coefficient of the sample with the monolayer (R_{ML}) and the reflection coefficient of the substrate (R_S) so that $\Delta R = (R_{ML} - R_S)/R_S$. The PL images are recorded by a Hamamatsu Fusion-BT CMOS camera. For STEM investigation, the samples were transferred to Quantifoil^{tm} grids using PMMA assisted transfer protocol. The high-angle annular dark-field scanning transmission electron microscopy (HAADF-STEM) image was acquired with a Thermofisher Talos 200X microscope operated at 200 kV. TERS and TEPL are carried out with state-of-the-art commercial system (Trios OmegaScope-R coupled with LabRAM spectrometer, Horiba Scientific). Silver coated tips with an apex radius of 20 nm were use for tip enhanced measurements. More details on experimental set-ups and procedures are given in the supplement.

DATA AVAILABILITY

The data that support the findings of this study are available from the corresponding authors upon request.

Received: 13 April 2022; Accepted: 14 October 2022;
Published online: 19 November 2022

REFERENCES

1. Splendiani, A. et al. Emerging photoluminescence in monolayer MoS_2. *Nano Lett.* **10**, 1271 (2010).
2. Mak, K. F., Lee, C., Hone, J., Shan, J. & Heinz, T. F. Atomically thin MoS_2: a new direct-gap semiconductor. *Phys. Rev. Lett.* **105**, 136805 (2010).
3. Tonndorf, P. et al. Photoluminescence emission and raman response of monolayer MoS_2, $MoSe_2$, and WSe_2. *Opt. Express* **21**, 4908–4916 (2013).
4. Kennes, D. M. et al. Moiré heterostructures as a condensed-matter quantum simulator. *Nat. Phys.* **17**, 155–163 (2021).
5. Gu, J. et al. Dipolar excitonic insulator in a moire lattice. *Nat. Phys.* **18**, 395–400 (2022).
6. Li, H. et al. Imaging two-dimensional generalized wigner crystals. *Nature* **597**, 650–654 (2021).
7. Wang, J., Verzhbitskiy, I. & Eda, G. Electroluminescent devices based on 2d semiconducting transition metal dichalcogenides. *Adv. Mater.* **30**, 1802687 (2018).
8. Novoselov, K. S., Mishchenko, A., Carvalho, A. & Castro Neto, A. H. 2d materials and van der waals heterostructures. *Science* **353**, aac9439 (2016).
9. Mak, K. F. & Shan, J. Photonics and optoelectronics of 2d semiconductor transition metal dichalcogenides. *Nat. Photonics* **10**, 216–226 (2016).
10. Schaibley, J. R. et al. Valley depolarization dynamics and valley hall effect of excitons in monolayer and bilayer MoS_2. *Nat. Rev. Mater.* **1**, 16055 (2016).
11. Unuchek, D. et al. Room-temperature electrical control of exciton flux in a van der waals heterostructure. *Nature* **560**, 340 (2018).
12. Schneider, C., Glazov, M. M., Korn, T., Höfling, S. & Urbaszek, B. Two-dimensional semiconductors in the regime of strong light-matter coupling. *Nat. Commun.* **3**, 2695 (2018).
13. Koperski, M. et al. Optical properties of atomically thin transition metal dichalcogenides: observations and puzzles. *Nanophotonics* **6**, 1289–1308 (2017).
14. Dufferwiel, S. et al. Valley-addressable polaritons in atomically thin semiconductors. *Nat. Photonics* **11**, 497 (2017).
15. Scuri, G. et al. Large excitonic reflectivity of monolayer $MoSe_2$ encapsulated in hexagonal boron nitride. *Phys. Rev. Lett.* **120**, 037402 (2018).
16. Hong, X. et al. Ultrafast charge transfer in atomically thin MoS_2/WS_2 heterostructures. *Nat. Nanotechnol.* **9**, 682 (2014).
17. Turunen, M. et al. Quantum photonics with layered 2D materials. *Nat. Rev. Phys.* **4**, 219–236 (2022).

18. Geim, A. K. & Grigorieva, I. V. Van der waals heterostructures. *Nature* **499**, 419–425 (2013).
19. Shree, S., Paradisanos, I., Marie, X., Robert, C. & Urbaszek, B. Guide to optical spectroscopy of layered semiconductors. *Nat. Rev. Phys.* **3**, 39–54 (2021).
20. Andrei, E. Y. et al. The marvels of moiré materials. *Nat. Rev. Mater.* **6**, 201–206 (2021).
21. Lu, A.-Y. et al. Janus monolayers of transition metal dichalcogenides. *Nat. Nanotechnol.* **12**, 744–749 (2017).
22. Zheng, T. et al. Excitonic dynamics in janus MoSSe and WSSe monolayers. *Nano Lett.* **21**, 931–937 (2021).
23. Petrić, M. M. et al. Raman spectrum of janus transition metal dichalcogenide monolayers WSSe and MoSSe. *Phys. Rev. B* **103**, 035414 (2021).
24. Gan, Z. et al. Chemical vapor deposition of high-optical-quality large-area monolayer Janus transition metal dichalcogenides. *Adv. Mater.* **34**, 2205226 (2022).
25. Najafidehaghani, E. et al. 1d p-n junction electronic and optoelectronic devices from transition metal dichalcogenide lateral heterostructures grown by one-pot chemical vapor deposition synthesis. *Adv. Funct. Mater.* **31**, 210108 (2021).
26. Huang, C. et al. Lateral heterojunctions within monolayer $MoSe_2$-WSe_2 semiconductors. *Nat. Mater.* **13**, 1096–1101 (2014).
27. Duan, X. et al. Lateral epitaxial growth of two-dimensional layered semiconductor heterojunctions. *Nat. Nanotechnol.* **9**, 1024–1030 (2014).
28. Gong, Y. et al. Vertical and in-plane heterostructures from WS_2/MoS_2 monolayers. *Nat. Mater.* **13**, 1135–1142 (2014).
29. Wu, W. et al. Self-powered photovoltaic photodetector established on lateral monolayer MoS_2-WS_2 heterostructures. *Nano Energy* **51**, 45–53 (2018).
30. Pospischil, A., Furchi, M. M. & Mueller, T. Solar-energy conversion and light emission in an atomic monolayer p–n diode. *Nat. Nanotechnol.* **9**, 257–261 (2014).
31. Sahoo, P. K., Memaran, S., Xin, Y., Balicas, L. & Gutiérrez, H. R. One-pot growth of two-dimensional lateral heterostructures via sequential edge-epitaxy. *Nature* **553**, 63–67 (2018).
32. Wang, J., Li, Z., Chen, H., Deng, G. & Niu, X. Recent advances in 2d lateral heterostructures. *Nanomicro Lett* **11**, 1–31 (2019).
33. Li, M.-Y. et al. Epitaxial growth of a monolayer WSe_2-MoS_2 lateral pn junction with an atomically sharp interface. *Science* **349**, 524–528 (2015).
34. Zhang, Y. et al. Edge-epitaxial growth of 2d NbS_2-WS_2 lateral metal-semiconductor heterostructures. *Adv. Mater.* **30**, 1803665 (2018).
35. Mahjouri-Samani, M. et al. Patterned arrays of lateral heterojunctions within monolayer two-dimensional semiconductors. *Nat. Commun.* **6**, 7749 (2015).
36. Chu, Y.-H. et al. Atomic scale depletion region at one dimensional $MoSe_2$-WSe_2 heterointerface. *Appl. Phys. Lett.* **113**, 241601 (2018).
37. Guo, Y. & Robertson, J. Band engineering in transition metal dichalcogenides: stacked versus lateral heterostructures. *Appl. Phys. Lett.* **108**, 233104 (2016).
38. Lau, K. W. et al. Interface excitons at lateral heterojunctions in monolayer semiconductors. *Phys. Rev. B* **98**, 115427 (2018).
39. Taniguchi, T. & Watanabe, K. Synthesis of high-purity boron nitride single crystals under high pressure by using ba-bn solvent. *J. Cryst. Growth* **303**, 525–529 (2007).
40. Rhodes, D., Chae, S. H., Ribeiro-Palau, R. & Hone, J. Disorder in van der waals heterostructures of 2d materials. *Nat. Mater.* **18**, 541 (2019).
41. Raja, A. et al. Dielectric disorder in two-dimensional materials. *Nat. Nanotechnol.* **14**, 832–837 (2019).
42. Cadiz, F. et al. Excitonic linewidth approaching the homogeneous limit in MoS_2-based van der waals heterostructures. *Phys. Rev. X* **7**, 021026 (2017).
43. Ajayi, O. A. et al. Approaching the intrinsic photoluminescence linewidth in transition metal dichalcogenide monolayers. *2D Mater.* **4**, 031011 (2017).
44. Wierzbowski, J. et al. Direct exciton emission from atomically thin transition metal dichalcogenide heterostructures near the lifetime limit. *Sci. Rep.* **7**, 12383 (2017).
45. Stier, A. V. et al. Magnetooptics of exciton rydberg states in a monolayer semiconductor. *Phys. Rev. Lett.* **120**, 057405 (2018).
46. Shree, S. et al. High optical quality of MoS_2 monolayers grown by chemical vapor deposition. *2D Mater.* **7**, 015011 (2019).
47. Paradisanos, I. et al. Controlling interlayer excitons in MoS_2 layers grown by chemical vapor deposition. *Nat. Commun.* **11**, 2391 (2020).
48. Martin, E. W. et al. Encapsulation narrows and preserves the excitonic homogeneous linewidth of exfoliated monolayer $MoSe_2$. *Phys. Rev. Appl.* **14**, 021002 (2020).
49. Liu, J. Scanning transmission electron microscopy and its application to the study of nanoparticles and nanoparticle systems. *J. electron microsc. tech.* **54**, 251–278 (2005).
50. Jia, H. et al. Large-scale arrays of single-and few-layer MoS_2 nanomechanical resonators. *Nanoscale* **8**, 10677–10685 (2016).
51. Shree, S. et al. Observation of exciton-phonon coupling in $MoSe_2$ monolayers. *Phys. Rev. B* **98**, 035302 (2018).
52. Wang, G. et al. In-plane propagation of light in transition metal dichalcogenide monolayers: optical selection rules. *Phys. Rev. Lett.* **119**, 047401 (2017).
53. He, M. et al. Valley phonons and exciton complexes in a monolayer semiconductor. *Nat. Commun.* **11**, 618 (2020).
54. Brem, S. et al. Phonon-assisted photoluminescence from indirect excitons in monolayers of transition-metal dichalcogenides. *Nano Lett.* **20**, 2849–2856 (2020).
55. Delhomme, A. et al. Magneto-spectroscopy of exciton rydberg states in a cvd grown WSe_2 monolayer. *Appl. Phys. Lett.* **114**, 232104 (2019).
56. Soubelet, P., Bruchhausen, A. E., Fainstein, A., Nogajewski, K. & Faugeras, C. Resonance effects in the raman scattering of monolayer and few-layer $MoSe_2$. *Phys. Rev. B* **93**, 155407 (2016).
57. McDonnell, L. P., Viner, J. J., Rivera, P., Xu, X. & Smith, D. C. Observation of intravalley phonon scattering of 2s excitons in $MoSe_2$ and WSe_2 monolayers. *2D Mater.* **7**, 045008 (2020).
58. Cadiz, F. et al. Exciton diffusion in Wse_2 monolayers embedded in a van der waals heterostructure. *Appl. Phys. Lett.* **112**, 152106 (2018).
59. Kulig, M. et al. Exciton diffusion and halo effects in monolayer semiconductors. *Phys. Rev. Lett.* **120**, 207401 (2018).
60. Rosati, R. et al. Dark exciton anti-funneling in atomically thin semiconductors. *Nat. Commun.* **12**, 7221 (2021).
61. Zhang, X.-X., You, Y., Zhao, S. Y. F. & Heinz, T. F. Experimental evidence for dark excitons in monolayer WSe_2. *Phys. Rev. Lett.* **115**, 257403 (2015).
62. Robert, C. et al. Fine structure and lifetime of dark excitons in transition metal dichalcogenide monolayers. *Phys. Rev. B* **96**, 155423 (2017).
63. Wang, G. et al. Spin-orbit engineering in transition metal dichalcogenide alloy monolayers. *Nat. Commun.* **6**, 10110 (2015).
64. Lu, Z. et al. Magnetic field mixing and splitting of bright and dark excitons in monolayer $MoSe_2$. *2D Mater.* **7**, 015017 (2019).
65. Robert, C. et al. Measurement of the spin-forbidden dark excitons in MoS_2 and $MoSe_2$ monolayers. *Nat. Commun.* **11**, 4037 (2020).
66. Lee, H. et al. Tip-enhanced photoluminescence nano-spectroscopy and nano-imaging. *Nanophotonics* **9**, 3089–3110 (2020).
67. Darlington, T. P. et al. Imaging strain-localized excitons in nanoscale bubbles of monolayer WSe_2 at room temperature. *Nat. Nanotechnol.* **15**, 854–860 (2020).
68. Zhang, S. et al. Nano-spectroscopy of excitons in atomically thin transition metal dichalcogenides. *Nat. Commun.* **13**, 542 (2022).
69. Poumirol, J.-M. et al. Unveiling the optical emission channels of monolayer semiconductors coupled to silicon nanoantennas. *ACS Photonics* **7**, 3106–3115 (2020).
70. Schmidt, R. et al. Reversible uniaxial strain tuning in atomically thin WSe_2. *2D Mater.* **3**, 021011 (2016).
71. Farkous, M. et al. Strain effects on the electronic and optical properties of van der waals heterostructure MoS_2/WS_2: A first-principles study. *Physica E Low Dimens. Syst. Nanostruct.* **116**, 113799 (2020).
72. Shimasaki, M. et al. Directional exciton-energy transport in a lateral hetero-monolayer of WSe_2-$MoSe_2$. *ACS Nano* **16**, 8205–8212 (2022).
73. Zheng, D. et al. Manipulating coherent plasmon-exciton interaction in a single silver nanorod on monolayer WSe_2. *Nano Lett.* **17**, 3809–3814 (2017).
74. Chen, P. et al. Approaching the intrinsic exciton physics limit in two-dimensional semiconductor diodes. *Nature* **599**, 404–410 (2021).
75. Shanks, D. N. et al. Interlayer exciton diode and transistor. *Nano Lett.* **22**, 6599–6605 (2022).
76. Butov, L. Excitonic devices. *Superlattices Microstruct.* **108**, 2–26 (2017).

ACKNOWLEDGEMENTS

Toulouse acknowledges partial funding from ANR IXTASE, ANR HiLight, ANR Ti-P, NanoX project 2DLight, the Institut Universitaire de France, and the EUR grant ATRAP-2D NanoX ANR-17-EURE-0009 in the framework of the "Programme des Investissements d'Avenir", the Institute of quantum technology in Occitanie IQO and a UPS excellence PhD grant. Growth of hexagonal boron nitride crystals was supported by JSPS KAKENHI (Grants No. 19H05790, No. 20H00354 and No. 21H05233). The Jena group received financial support of the Deutsche Forschungsgemeinschaft (DFG) through a research infrastructure grant INST 275/257-1 FUGG, CRC 1375 NOA (Project B2), SPP2244 (Project TU149/13-1) as well as DFG grant TU149/16-1. This project has also received funding from the joint European Union's Horizon 2020 and DFG research and innovation programme FLAG-ERA under grant TU149/9-1.

AUTHOR CONTRIBUTIONS

Z.G., E.N., A.G. and A.T. developed the growth method and fabricated the lateral heterostructures. T.T. and K.W. grew the hBN crystals. D.B., L.L., and P.R. performed and analyzed exciton transport experiments. U.K., T.L., J.B. performed and analyzed transmission electron microscopy. I.P. and S.S. carried out hBN encapsulation. I.P., S.S., A.E.-R., D.L., X.M., B.U. performed and interpreted PL, Raman and reflectivity experiments. H.L. and J.-M.P. performed TEPL and TERS. S.W., V.P. and J.-M.P. optimized the TEPL and TERS set-up. D.B., H.L., J.-M.P. and L.L. performed the numerical modeling. L.L., J-M.P., A.T., and B.U. wrote the manuscript with inputs from all the authors and supervised the project.

FUNDING

Open Access funding enabled and organized by Projekt DEAL.

COMPETING INTERESTS

The authors declare no competing interests.

ADDITIONAL INFORMATION

Supplementary information The online version contains supplementary material available at https://doi.org/10.1038/s41699-022-00354-0.

Correspondence and requests for materials should be addressed to Laurent Lombez, Jean-Marie Poumirol, Andrey Turchanin or Bernhard Urbaszek.